Measurements of the trapped particle sideband instability compared to the macroparticle model

D. A. Hartmann[a] and C. F. Driscoll
Physics Department, University of California at San Diego, La Jolla, California 92093

(Received 22 January 2001; accepted 20 April 2001)

The upper and lower sidebands are measured on a traveling wave tube where a cold electron beam is trapped by a large amplitude wave. The two strongly coupled sidebands form a normal mode that is characterized by the sideband growth rates, wave number shifts, amplitude ratio, and phase relationship. The measured values agree only qualitatively with the macroparticle model of Kruer, Dawson, and Sudan [Phys. Rev. Lett. **23**, 838 (1969)]. Also, the macroparticle model prediction for a nonlinear product wave does not agree with the experiment. Quantitative agreement is found between the experiment and computer simulations that follow the electron orbits, suggesting that the trapped particle model is too simple for quantitative predictions. © *2001 American Institute of Physics.* [DOI: 10.1063/1.1379341]

I. INTRODUCTION

It is well known, both experimentally and theoretically, that the nonlinear motion of electrons trapped in the field of a large amplitude plasma wave causes waves at nearby lower and higher frequencies to become unstable. These waves are called sidebands. Sideband growth was first observed by Wharton, Malmberg, and O'Neil[1] when launching a large amplitude wave in a Maxwellian plasma, and later verified in similar experiments.[2–8] Sideband growth has also been observed after saturation of a weak cold beam–plasma instability,[9–15] in free electron lasers (FELs)[16–18] and in high power traveling wave tubes (TWTs).[19] The interaction of the beam with electrostatic waves on the TWT is similar to the interaction of a weak cold beam with electrostatic waves in a plasma, since the main role of the plasma is to support the waves as a linear dielectric. In FELs, the growth of parasitic sideband waves is one of the main mechanisms that limit the performance of the amplifier, since these waves become large enough to detrap the electrons, preventing further gain. Numerous authors have also investigated the sideband instability in computer simulations.[20–25] The mechanisms and properties of the sideband growth are therefore of continued interest.

Two different mechanisms have been identified that contribute to sideband growth. If the large amplitude wave decays within few trapping oscillations (e.g., when launched in a Maxwellian plasma) then a fraction of the initially trapped electrons becomes untrapped. This can lead to a time-averaged electron velocity distribution function that is unstable to the growth of waves at nearby frequencies.[7,9] If, however, the large amplitude wave undergoes several trapping oscillations without significant damping (e.g., after saturation of a weak cold beam–plasma instability) then a nonlinear trapped electron distribution can arise that is unstable to the growth of waves at nearby frequencies. This situation is the focus of this study.

A fruitful simplification of the highly nonlinear trapped-particle distribution is the macroparticle model (MPM) by Kruer, Dawson, and Sudan:[26] They consider the trapped electrons only, and approximate them as a macroparticle in a harmonic well. That is, the large amplitude wave with frequency ω_T and phase velocity v_T has trapped a single macroparticle, which ''bounces'' (oscillates) at frequency ω_B in the trapping wave. Self-consistently coupling the oscillations of the macroparticle to small sidebands gives a dispersion relation that has unstable solutions for both upper (u) and lower (l) sidebands. The condition for instability is

$$\omega_u - k_u^r v_T \approx -\omega_B , \tag{1}$$

$$\omega_l - k_l^r v_T \approx \omega_B . \tag{2}$$

Here, ω_u and ω_l are the sideband frequencies, and k_u^r and k_l^r are the real parts of the sideband wave numbers.

Physically, Eqs. (1) and (2) state that the sidebands are unstable if their frequencies, when Doppler shifted into the frame of the trapped macroparticle, equal the bounce frequency. In this dispersion relation, also referred to as sideband resonance condition, the upper and lower sidebands are coupled together to form a normal mode. Obviously, the macroparticle approximation is crude[27,28] and other authors have since improved on it by including untrapped particles[29] and by investigating its range of applicability.[28] However, the MPM is intriguing in its simplicity and physical insight, and thus warrants detailed comparison with experiment. This is the purpose of this article.

Morales[27] found a particularly promising trapped electron state to which the MPM could be applied. He considered a dc electric field along the propagation direction of an electron beam interacting with a damped, electrostatic wave. Computer simulations showed cases where the beam is partially trapped in the potential well of the wave. After a few trapping oscillations, an asymptotic state of constant wave

[a]Present address: Max-Planck Institute for Plasma Physics, 85478 Garching, Germany.

amplitude was reached, where the energy gain of the trapped electrons in the dc electric field balanced the energy loss of the damped wave. The highly nonlinear state was also characterized by a lower phase velocity of the trapping wave compared to the beamless case. Morales suggested that the phase-space structure of the trapped electrons is sufficiently localized to approximate it as a macroparticle of some effective charge, so the MPM should predict the properties of sideband wave growth.

We generate and investigate these asymptotic trapped-particle states in both experiments and computer simulations. For our experiments we use a traveling wave tube (TWT) where a monoenergetic electron beam is trapped by a launched large amplitude wave, with a dc electric field applied along the axis of the experiment. By suitably choosing the launch level of the trapping wave, we can obtain states of spatially constant amplitude. We find that the measured fraction of trapped electrons agrees with the prediction of the MPM, while the measured wave number shift of the large amplitude wave is smaller than predicted.

We investigate this trapped particle state by additionally launching small amplitude lower and upper sideband waves. The sidebands are linear in that their spatial evolution depends only on the ratio of their amplitudes and their phase relationship. Thus, they cause only linear perturbations in the motion of the trapped electrons.

The sidebands are observed to grow for frequencies that approximately fulfill Eqs. (1) and (2), where the bounce frequency is calculated from the trapping wave amplitude. The sidebands are strongly coupled through the trapped electrons if the sidebands and the trapping wave have approximately the same phase velocity. This coupling makes the sidebands appear to be a single normal mode. The measured sideband growth rates, the changes to their wave numbers, and the amplitude ratio and phase relationship of the sideband normal modes agree only qualitatively with the predictions of the MPM. Better quantitative agreement is found between the experiment and computer simulations that more precisely follow the orbits of the beam electrons. Therefore we conclude that the discrepancy between the measured properties of the sideband modes and the predictions of the MPM are caused by the model's simplification of the phase-space orbits of the trapped electrons. In addition, we find that the properties of a growing ''difference'' wave observed at the frequency of the sideband frequency separation are not properly predicted by the MPM.

The remainder of this article is organized as follows. In Sec. II we briefly describe the experimental setup and its operation. In Sec. III we recall the theory of the TWT, relate the properties of the macroparticle to measurable quantities, formulate the sideband dispersion relation for the TWT, and describe the properties of the sideband normal mode solution. In Sec. IV we present our experiments and computer simulations for a case with spatially constant trapping wave amplitude. In Sec. V the sideband properties are compared with the predictions of the MPM. In Sec. VI we summarize our results.

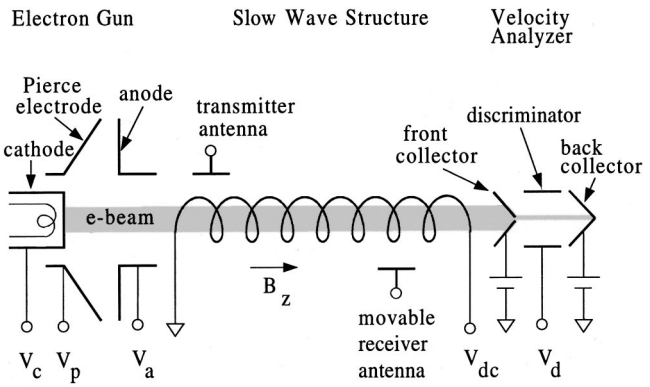

FIG. 1. Schematic of the traveling wave tube.

II. EXPERIMENT

Figure 1 shows a schematic of the traveling wave tube,[30] which has been described in detail elsewhere.[14,31–33] The TWT consists of three main elements: an electron gun, a helical slow wave structure with axially movable antennas, and an electron velocity analyzer. The electron gun creates a beam with adjustable axial velocities and currents; this beam propagates along the axis of the helix, in a field $B_z = 420\,\mathrm{G}$. Waves launched with a transmitter antenna at the gun end of the helix travel along the helix and continuously interact with the electron beam. The wave evolution is measured with a movable receiver antenna, and the final beam velocity distribution is measured with the velocity analyzer at the end of the interaction region.

The helix is about 2.7 m long, and composed of beryllium–copper wire glued to four exterior supporting alumina rods which are contained within a glass vacuum tube. Launched electromagnetic waves travel along the wire at the speed of light; their phase velocities v^{ph} along the z axis are smaller by approximately the tangent of the pitch angle, giving $v^{\mathrm{ph}} \approx 4 \times 10^6$ m/s. At both ends of the helix, resistive terminations reduce the reflections of the waves. The voltage standing wave ratio is about 1.26, due to residual end reflections and irregularities of the helix. Fortunately, the backward-traveling waves are far from resonance with the electrons, so their effect on the wave–beam instabilities can be neglected. The helix assembly and vacuum tube are contained within a lengthwise-slotted cylindrical waveguide. In the cylinder but outside the glass tube, four axially movable capacitative antennas can excite or detect helix modes in the frequency range from 5 to 95 MHz. Only the helix modes are launched, since empty waveguide modes cannot propagate below 3.0 GHz.

The measured dispersion of the helix (without a beam) is shown in Fig. 2. The helix modes have electric field components along the axis of the helix; and their radial structure has been discussed by Dimonte and Malmberg.[14] Helix waves with frequencies of 10–90 MHz will interact resonantly with beam particles with axial velocities of 5.6–3.4 $\times 10^6$ m/s.

We have also measured the damping rates k_n^{0i} for these linear waves on the beamless helix. We find that they are only slightly damped: At 60 MHz the damping is about 9 dB

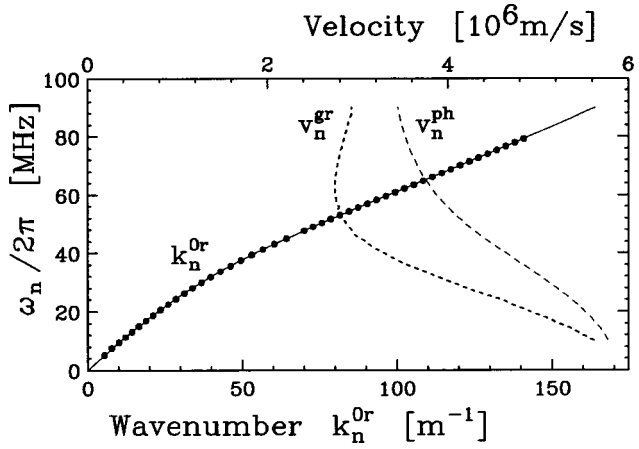

FIG. 2. Beamless helix dispersion relation $\omega_n(k_n^{0r})$, with phase velocity $v_n^{\rm ph}$ and group velocity $v_n^{\rm gr}$.

over the length of the helix, giving $k_n^{0i}/k_n^{0r} \approx 0.005$. Both wave number k_n^{0r} and damping rate k_n^{0i} depend only weakly on position: $\delta k_n^{0r}(z)/k_n^{0r} \approx \pm 0.5\%$ and $\delta k_n^{0i}(z)/k_n^{0i} \approx \pm 30\%$.

When an electron beam propagates with velocity v_b down the helix, it destabilizes those helix modes which have $v^{\rm ph} \approx v_b$. This helix is much longer than commercially available TWTs, allowing us to observe about 20 e-folding lengths of linear wave growth. This allows measurements of the evolution of launched waves well into the nonlinear regime.

The electron beam is obtained from a Pierce-type electron gun mounted at the front end of the helix. The indirectly heated dispenser cathode is biased at potential V_c, giving a beam with energy $1/2mv_b^2 = eV_c$. The Pierce electrode is biased at a slightly more negative potential to obtain an essentially monoenergetic electron beam with constant radial density. Once every 60th of a second, an 80 μs beam is obtained by pulsing the anode from a retarding voltage to an accelerating voltage V_a which is less negative than V_c. The voltage difference $V_a - V_c$ regulates the beam current. The beam is pulsed so that ions created from the residual background gas ($P \approx 10^{-6}$ Torr) do not accumulate and neutralize the beam. Typical beam currents are $I_b \lesssim 50\,\mu$A, and typical cathode voltages are $V_c \approx -50$ V. A static voltage $V_{\rm dc}$ applied to the helix gives a uniform electric field $E_{\rm dc}$ which tends to accelerate the beam electrons.

At the end of the helix, the time-averaged axial velocity distribution of the electron beam is measured with a retarding field velocity analyzer. The rf part of the velocity distribution function cannot be measured, because the electrons loose their phase relationship with the waves in the drift region between the end of the helix and the analyzer.

The TWT noise level is sufficiently low that waves can be launched well above the noise and still be much smaller than saturation. The full wave form is repeatedly launched with an arbitrary wave form generator at the gun end of the helix ($z=0$). We measure the spatial evolution of the waves by detecting and recording the temporal wave form at positions spaced 5 mm apart in z; then the amplitudes and phases of the trapping wave and the sidebands are obtained by Fourier transformation of the temporal wave forms. The accuracy of the measured amplitudes is about 2 dB, and the accuracy of the phases is about $\pi/5$.

The full electric field $E(z,t)$ is composed of waves at frequencies ω_n, so the full spatial evolution can be written as

$$E(z,t) = \sum_n |E_n(z)| \exp\{-i\tilde{\phi}_n(z,t)\} \tag{3}$$

with

$$|E_n(z)| = |E_n(0)| \exp\left\{ \int_0^z dz'\, k_n^i(z') \right\}, \tag{4}$$

$$\tilde{\phi}_n(z) \equiv \phi_n(z,t) - \omega_n t, \tag{5}$$

$$\phi_n(z) = \int_0^z dz'\, k_n^r(z') + \phi_n(0), \tag{6}$$

$$\equiv \int_0^z dz'\, k_n^{r0}(z') + \phi_n(0) + \delta\phi_n(z), \tag{7}$$

$$\delta\phi_n(z) \equiv \int_0^z dz'\, \delta k_n^r(z'). \tag{8}$$

We obtain the ''local'' growth rate $k_n^i(z)$ by fitting a straight line to the spatial evolution of the logarithm of the magnitude $|E_n(z)|$ of the wave electric field amplitude in some region around z. The interaction of the waves with the trapped electrons and with each other causes deviations in their wave numbers from the beamless case k_n^{0r}. We obtain the ''local'' wave number $k_n^r(z)$ by fitting a straight line to the phase $\phi_n(z)$ in some region around z. The wave number shift is then given by $\delta k_n(z) \equiv k_n^r(z) - k_n^{r0}(z)$. In both cases, the fit region is typically 0.25 m long, which corresponds to 2–5 wavelengths.

The launched electric field spectrum at $z=0$ typically consists of a large amplitude trapping wave $E_T(0)$ at frequency $f_T \equiv \omega_T/2\pi = 55.4$ MHz, and two small (upper and lower) sidebands with symmetric frequencies $\omega_{(u,l)} = \omega_T \pm \delta\omega_{\rm sb}$ and amplitudes $E_{(u,l)}(0)$. Launch phases, $\phi(0)$, and launch electric field amplitudes, $E(0)$, can be arbitrarily chosen. Here, (T,u,l) and (n) are alternate notations for the individual modes; and f and ω may both be used for any particular frequency.

III. THEORY

A. Traveling wave tube

The linear and nonlinear theory of the interaction of an electron beam with waves on a slow wave structure is well known.[14,31–33] The coupling of the beam to the waves is often given by a one-dimensional transmission line equation, which can be cast in the form of Poisson's equation:

$$ik_n(z)\epsilon_0 \epsilon^h(\omega_n, k_n(z)) E_n(z) = \rho_n(z), \tag{9}$$

$$\epsilon^h(\omega_n, k_n) = (k_n^{02} - k_n^2)/\epsilon_0 \omega k_n^0 k_n^2 R_n A_b. \tag{10}$$

Here, $\epsilon^h(\omega_n,k_n(z))$ is the ''helix dielectric;'' R_n is the beam–wave interaction impedance[30] at frequency ω_n, which ranges between 500 and 1800 Ω for our TWT; A_b is the beam cross-sectional area; and $\rho_n(z)$ is the Fourier component of the axial beam charge density at frequency ω_n. Setting $\epsilon^h(\omega_n,k_n)=0$ yields the dispersion of the helix waves, i.e., $k_n^0(\omega_n)$. These are the waves that are supported by the helix in absence of an electron beam. As shown in Fig. 2, they have a dispersion similar to electrostatic Gould–Trivelpiece waves in a warm plasma of finite extent. Theoretical predictions of the wave number and the strength of the coupling of the beam to the helix modes agree within ±1% and ±10%, respectively with the experimental measurements.[31,32]

The velocity of the beam electrons, $v(z,t)$, is given by Newton's equation:

$$\frac{dv}{dt}=-\frac{e}{m}(E(z,t)+E_{\rm sc}(z,t)+E_{\rm dc}). \tag{11}$$

Here, $E_{\rm sc}(z,t)$ is the ''space-charge'' electric field, generated by the beam electrons. In a plasma this field is shielded out; in a traveling wave tube it typically is small compared to the wave electric field E. $E_{\rm dc}$ is the externally applied dc electric field. Equations (9) and (11), together with the beam continuity equation

$$i\omega_n\rho_n=\frac{\partial}{\partial z}(v\rho_n), \tag{12}$$

completely describe the spatial evolution of the wave–beam interaction.

To follow the evolution into the nonlinear regime, we solve Eqs. (9)–(12) numerically by modeling the beam as a collection of charged disks. In these simulations we include the space-charge and higher order terms. The methods of solution are described elsewhere.[25,31,32]

B. Trapped macroparticle state

Within the macroparticle model, the asymptotic trapped electron state is characterized by the following parameters: the effective charge of the macroparticle, $\sigma I_b/f_T$; its center-of-mass velocity v_T; its phase relative to the trapping wave, $\Delta\Theta$; and its bounce frequency ω_B in the superposition of trapping wave potential and applied dc potential. In the experiment, we can obtain all these parameters from measured quantities once a steady state has been reached.

Following Morales, we divide the beam electrons into the fraction σ that is trapped in the trapping wave potential, and the fraction $1-\sigma$ that is not trapped. The untrapped electrons can be neglected for the evolution of the sidebands, because the applied dc electric field quickly accelerates them to velocities higher than the highest wave phase velocity in the TWT.

Conservation of trapped electron and wave momentum in the asymptotic steady state gives the effective charge of the macroparticle as[27,32]

$$\frac{\sigma I_b}{f_T}=\frac{1}{f_T}k_T^{0i}\frac{E_T^{\infty 2}}{k_T^{0r2}R_T E_{\rm dc}}. \tag{13}$$

Here, E_T^∞ is the asymptotic steady state amplitude of the trapping wave electric field. In steady state the asymptotic wave number of the trapping wave, k_T^∞, is given by

$$k_T^\infty=k_T^{0r}+k_T^{0i}\sqrt{\left(\frac{E_T^\infty}{E_{dc}}\right)^2-\sigma^2}. \tag{14}$$

From energy balance in the asymptotic state, we require the center-of-mass velocity of the macroparticle, v_T, to equal the asymptotic phase velocity of the trapping wave given by

$$v_T^\infty=\omega_T/k_T^\infty, \tag{15}$$

Due to the applied dc electric field, the equilibrium position of the macroparticle is shifted by

$$\Delta\Psi=\arcsin\left(\frac{E_{\rm dc}}{E_T^\infty}\right) \tag{16}$$

compared to the trapping wave potential minimum; the shift is in the direction opposite to the externally applied field. The bounce frequency of the macroparticle is given by

$$\omega_B^{\rm dc}\equiv\left[1-\left(\frac{E_{\rm dc}}{E_T^\infty}\right)^2\right]^{1/4}\sqrt{\frac{eE_T^\infty k_T^\infty}{m}}. \tag{17}$$

C. Macroparticle model

We apply the analysis of Kruer, Dawson, and Sudan to the spatial evolution of sidebands for the asymptotic trapped particle state. To this end, we model the electrons as an array of harmonically bound (with bounce frequency ω_B) macroparticles of charge $\sigma I_b/f_T$ that move with velocity v_T^∞. Initially, the macroparticles are at rest in the frame of the trapping wave. Sideband waves of small amplitude can disturb the macroparticles from their equilibrium position, and this changed charge distribution can in turn cause wave growth. A self-consistent description leads to a set of equations that couple the electric field amplitudes of different frequencies.

This set of equations is truncated by limiting the coupling to lower and upper sidebands at frequencies $\omega_l=\omega_T-\delta\omega_{\rm sb}$ and $\omega_u=\omega_T+\delta\omega_{\rm sb}$. The dispersion relation for this model is then given by

$$\frac{\sigma\omega_p^2}{(kv_T-\omega)^2-\omega_B^2}\left[\frac{\omega/kv_T}{\epsilon^h(\omega,k)}+\frac{(\omega-2\omega_T)/(k-2k_T)v_T}{\epsilon^h(\omega-2\omega_T,k-2k_T^\infty)}\right]=1, \tag{18}$$

where $\omega_p^2=I_b e/A_b v_T\epsilon_0 m$ is the beam plasma frequency squared. For some values of $\delta\omega_{\rm sb}$, one finds growing roots of this dispersion relation, i.e., $k\equiv k^r-ik^i$ with $k^i>0$ at the frequencies $\omega=\omega_T\pm\delta\omega_{\rm sb}$. We call these roots ''sideband normal modes.'' The growth rates of both sidebands are identical ($k_u^i=k_l^i$), and their wave numbers (k_u^r, k_l^r) are related by

$$k_u^r+k_l^r=2k_T^\infty. \tag{19}$$

In addition, the sideband normal modes predict that there exists a particular relationship between the complex amplitudes of the upper and the lower sidebands, given by

$$\frac{E_u^*}{E_l}=\left[\frac{kv_T}{\omega_p}\frac{\epsilon^h(k_u,\omega)}{\omega_p^2}((\omega-k_uv_T)^2-\omega_B^2)-1\right]\equiv\alpha e^{i\theta}. \tag{20}$$

Here, $\alpha(z)$ is the ''sideband amplitude ratio'' and $\theta(z)$ is the sideband phase difference, which will be related to the ''modulational phase'' [32] Θ defined in the following. (Note that Θ is also called the ''invariant phase'' by Tsunoda and Malmberg.)[25] In Sec. IV we compare the measured growth rates and wave numbers of the sidebands, their amplitude ratio, and phase relationship with the predictions of the model.

The modulational phase Θ of the two sidebands is easily measured and has physical relevance: If $\Theta=0$, the superposition of the three waves is an amplitude modulated trapping wave; whereas if $\Theta=\pi$, the superposition is a frequency modulated trapping wave. Using Eq. (7) we define the modulational phase as

$$\Theta(z)\equiv 2\phi_T(z)-\phi_l(z)-\phi_u(z) \tag{21}$$

$$=\int_0^z dz'[(2k_T^r(z')-k_l^r(z')-k_u^r(z'))]+2\phi_T(0)$$

$$-\phi_l(0)-\phi_u(0). \tag{22}$$

Note that $\Theta(z)$ is time independent, because the frequencies of the upper and lower sidebands are symmetric to the trapping wave frequency ω_T. If the upper and lower sidebands form a sideband normal mode, then their wave numbers are related to one another through Eq. (19), and their phases are related through Eq. (20). In this case the integrand of Eq. (22) vanishes. With the small correction due to the shift $\Delta\Psi$ of the equilibrium position of the macroparticle in the dc electric field from Eq. (16), we obtain

$$\Theta(z)=\theta(z)+2\Delta\Psi(z). \tag{23}$$

IV. EXPERIMENTAL OBSERVATIONS

A. Trapped electron state

We trap the monoenergetic electron beam by launching the trapping wave at about the saturation level of the cold beam instability. The electron beam velocity approximately equals the phase velocity of the trapping wave, and we adjust the beam current and the applied dc field to obtain cases where the residual trapping oscillations are small, so a state of spatially constant wave number shift and amplitude is obtained.

The solid line in Fig. 3 shows the measured spatial evolution of the trapping wave amplitude. After $z\approx 1.5\,\mathrm{m}$, the amplitude is constant (within about 10%) and the wave number shift (not shown) is approximately constant. Therefore we assume that an asymptotic trapped particle state has been reached; for comparison with theory we take the spatially averaged values of $E_T^\infty=200\,\mathrm{V/m}$ and $k_T^\infty-k_T^{0r}=1.1\,\mathrm{m}^{-1}$. The dotted line in Fig. 2 shows the damping of the trapping wave if no beam is present, with $k_T^{0i}=-0.44\,\mathrm{m}^{-1}$.

The dashed line in Fig. 3 shows the evolution as predicted from the computer simulation. The agreement between experiment and simulation is good, since the spatial dependence of wave numbers and damping rates on the beamless helix are taken into account. The residual amplitude modulations near the end of the interaction region are predominantly caused by the spatial dependence of wave number and damping rate. Typically the steady-state values of the electric field amplitude agree within 15% and the steady-state values of the wave number shifts agree within $\pm 0.2\,\mathrm{m}^{-1}$.

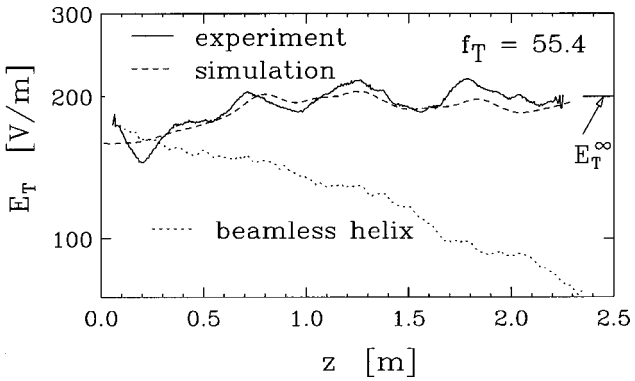

FIG. 3. Spatial evolution of the trapping wave in the experiment (solid) and in computer simulation (dashed). Wave evolution without a beam is also shown (dotted).

In the following, measurements of the growing sidebands are shown for this trapped particle state unless otherwise noted. The parameters of this case are: $f_T=55.4\,\mathrm{MHz}$, $I_b=50\mu\,\mathrm{A}$, $v_T=4\times10^6\,\mathrm{m/s}$, $E_{\mathrm{dc}}=40.4\,\mathrm{V/m}$.

Figure 4(a) shows the computed phase space distribution of the electrons at the end of the interaction region. The electron phase, $\delta\phi_e$, is plotted relative to the phase of the trapping wave. The electron distribution consists of a trapped

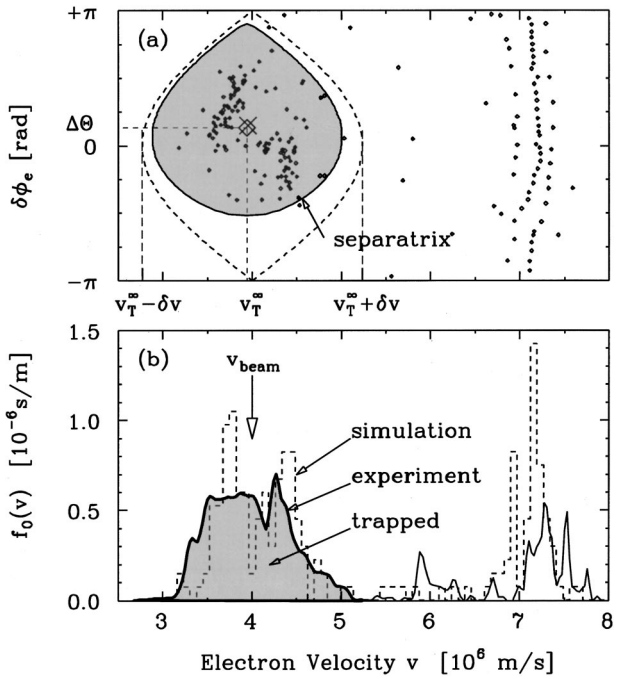

FIG. 4. (a) Phase-space plot of the simulation electrons at $z=2.3$. (b) Time-averaged velocity distribution from experiment (solid) and simulation (dashed).

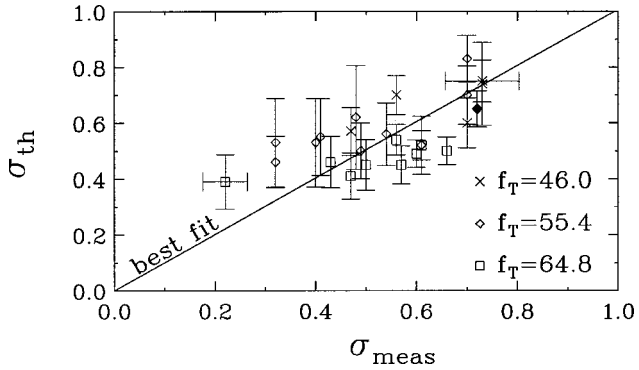

FIG. 5. Comparison of the measured trapped electron fraction σ_{meas} with σ_{th} from Eq. (13), for three trapping wave frequencies.

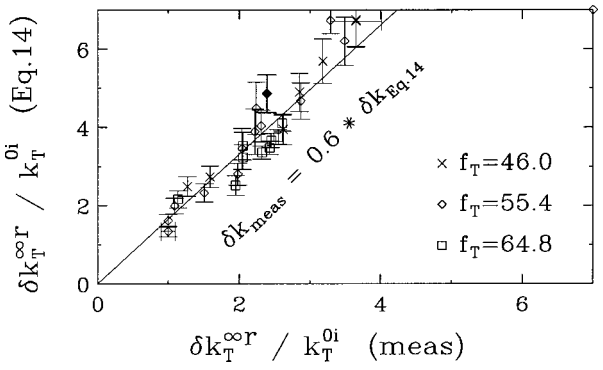

FIG. 6. Comparison of the measured wave number shift of the trapping wave with the wave number shift calculated from Eq. (14) of the MPM, for three trapping wave frequencies.

portion and a runaway portion. The separatrix of the trapping wave potential alone is shown as a dashed line; and the effective separatrix of the trapping wave plus the applied dc potential is shown as a solid line with a shaded interior. Most of the electrons that have not become runaways are confined within the effective separatrix. The open diamond shows the location of the ''center of mass'' of the trapped electrons. It agrees well with the prediction (×) based on Eqs. (15) and (16) of the macroparticle model.

In Fig. 4(b) we show the measured time-averaged axial velocity distribution at the end of the interaction region (solid line) and compare it to a velocity histogram of the computed phase space distribution of Fig. 4(a). Both distributions are characterized by a separation into trapped and runaway electrons. The shaded region of the experimental distribution identifies the trapped electrons, approximately given by $v_T - \delta v < v < v_T + \delta v$ where $\delta v = \sqrt{2eE_T^{\infty}/mk_T^{\infty}}$. We obtain the trapped particle fraction σ_{meas} from the measured velocity distribution, $f_0(v)$, by integrating the velocity distribution over the trapped electrons

$$\sigma_{\text{meas}} \equiv \int_{v_T^{\infty}-\delta v}^{v_T^{\infty}+\delta v} f_0(v)\,dv. \tag{24}$$

The error made by using the separatrix of the wave potential rather than the separatrix of the effective potential is small.

In Fig. 5 we compare the measured trapped particle fraction σ_{meas} to the trapped particle fraction σ_{th} calculated from Eq. (13), for varying wave amplitudes E_T at three different frequencies. The case of Fig. 3 is shown with a closed diamond. We used the experimentally determined electric field, E_T^{∞}, of the trapping wave amplitude spatially averaged near the end of the interaction region. The best fit line through the origin gives $\sigma_{\text{meas}} = 1.03\sigma_{\text{th}}$. That is, the measured trapped particle fraction, σ_{meas}, agrees closely with the MPM simulation.

In Fig. 6 we compare the measured wave number shift of the trapping wave, $\delta k_T^{\infty} = (k_T^{\infty} - k_T^{0r})/k_T^{0i}$ (scaled by the damping rate of the beamless helix), with the MPM prediction given by Eq. (14). The case of Fig. 3 is shown with a closed diamond. We find that the measured wave number shift is about 0.6 as large as expected from the MPM. The computer simulations also give a δk_T^{∞} about half as large as predicted by the MPM. Evidently, the spread distribution of trapped electrons causes less wave number shift of the trapping wave than would a bunched distribution, i.e., the MPM is qualitatively but not quantitatively correct for the wave number shift.

B. Evolution of the sidebands

Finally, we investigate the properties of small amplitude sideband pairs propagating on trapped particle states, with symmetric frequencies $f_{u,l} = f_T \pm \delta f_{\text{sb}}$. We find that the sideband evolution depends only on the launched modulational phase Θ and on the sideband amplitude ratio α. For example, the evolution is independent of the individual sideband phases if the modulational phase is kept constant. For a range of sideband frequencies, we find that the modulational phase and the sideband amplitude ratio take on approximately the same constant values after an initial transition region.

Figure 7 shows a typical case of the spatial evolution of the amplitudes and phases of the trapping wave and the sidebands. Here, the sidebands are above and below f_T by $\delta f_{\text{sb}} = 14.1$ MHz, and the initial phases and amplitudes are given by $\Theta(0) = \pi$ and $\alpha(0) = 1$. The downstream evolution of the sidebands shown in Fig. 7 (after $z \approx 1.5$ m) is characterized by approximately exponential wave growth and linear phase shifts. By fitting straight lines to the logarithm of the sideband amplitudes, we obtain the growth rates. The growth rates of the sidebands are approximately equal, with $k_u^i \approx k_l^i \approx 0.80\,\text{m}^{-1}$. The wave number shifts of the sidebands can be obtained by straight-line fits to the measured nonlinear phase $\delta\phi$.

The lighter lines in Fig. 7 show the calculated evolution of sidebands and trapping wave by solving the equations of motion. The space-charge term was kept in this case; otherwise the predicted wave number shift would have been larger by approximately $0.2\,\text{m}^{-1}$ than the measured shift. The computer simulations agree reasonably with the measured evolution.

Figures 8(a) and 8(b) show the spatial evolution of the modulational phase Θ and the sideband amplitude ratio α for a wide range of initial values. The two dashed lines in each plot represent $\alpha(0) = 1$ and $\Theta(0) = 0, \pi$. The five solid lines represent $\Theta(0) = \pi$ and $\alpha(0) = 0.25$, 0.5, 1, 2, 4. Evidently, the evolution converges to modulational phase and

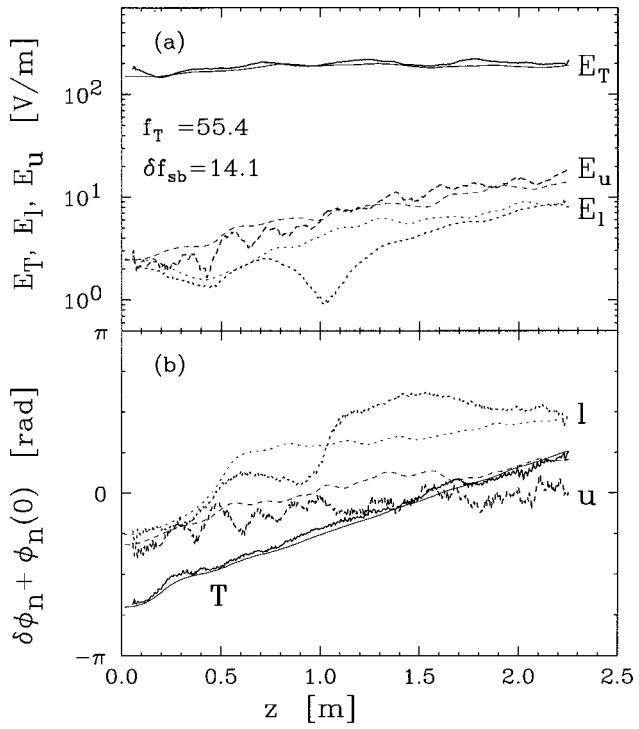

FIG. 7. Spatial evolution of the amplitudes E and phases ϕ of the trapping wave and sidebands, from measurements (dark) and simulation (thin). The sidebands have $\alpha=1$, $\Theta=-\pi$ at launch.

amplitude ratio values that are independent of the initial values. Also, the values of growth rate and wave number shift are approximately constant in the latter part of the evolutions, but this is not shown in Fig. 8.

For any given trapped particle state, we find a range of sideband separations δf_{sb} for which the modulational phase

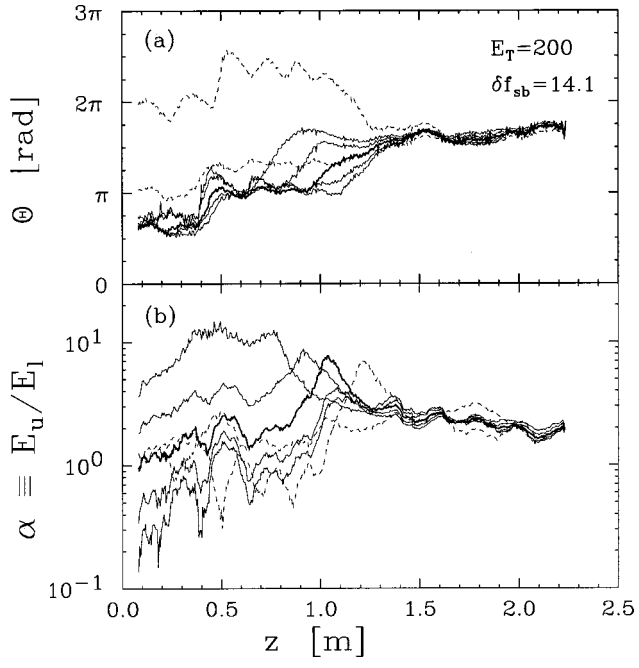

FIG. 8. Spatial evolution of the modulational phase Θ, and sideband amplitude ratio α, for different launch values. The dark lines correspond to the case shown in Fig. 7.

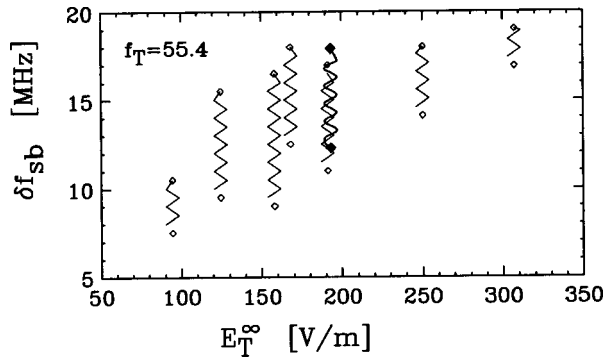

FIG. 9. Range of sideband frequency separation δf_{sb} for which a sideband normal mode is observed vs trapping wave amplitude E_T.

and sideband amplitude ratio converge to values independent of their launch values; over this range, a growing sideband normal mode exists and dominates the sideband evolution. For the trapping wave of Fig. 8, with $E_T^\infty=200$ V/m, this range is $11<\delta f_{sb}<17$ MHz. Figure 9 shows this range versus the trapping wave amplitude E_T^∞.

V. COMPARISON WITH THEORY

The experimental observations of the convergent modulational phases and amplitude ratios can be explained within the MPM as the dominance of the fastest growing sideband normal mode. The normal modes are characterized by particular values of modulational phase and amplitude ratio. Since in the experiment the sideband amplitudes are small, different sideband normal modes can superpose. At launch, the various sideband normal modes are excited to different extents, depending on the initial values of modulational phase and amplitude ratio; but during the interaction region, the fastest growing sideband normal mode eventually becomes dominant. Then only the modulational phase and sideband amplitude ratio of the dominant mode is measured.

In this section, we compare the experimentally determined properties of this growing sideband normal mode with the predictions of the macroparticle model and with computer simulations. In general, we find qualitative agreement between the predictions of the macroparticle model and the experiment, and close quantitative agreement between the computer simulations and experiment. In particular, we find (1) that the macroparticle model predicts the fastest growing sidebands at larger frequency separations than experimentally observed; (2) that the predicted growth rates, wave number shifts, and modulational phases are larger than those measured; (3) that a single normal mode only becomes dominant if the necessary wave number changes of the sidebands are small, whereas there is no such requirement in the sideband dispersion relation; and (4) that the observed difference wave at frequency δf_{sb} exhibits no coupling to the sidebands, whereas the MPM predicts coupling.

A. Frequency separation of the fastest growing sideband normal mode

According to the MPM, the frequencies of the fastest growing sidebands are direct indicators of the macroparticle

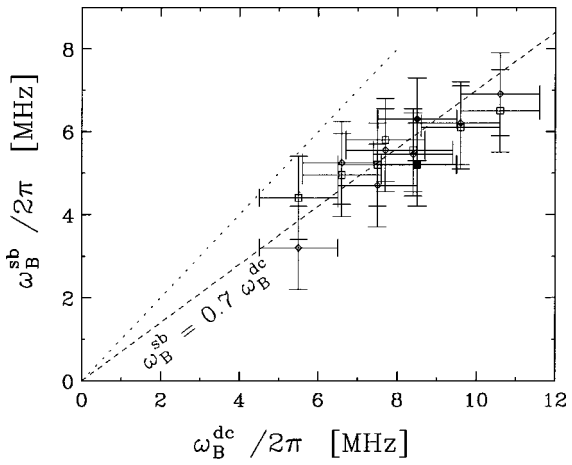

FIG. 10. Bounce frequency ω_B^{sb} inferred from the fastest growing sideband frequencies using Eqs. (1) and (2), vs bounce frequency ω_B^{dc} calculated from Eq. (17) using E_T and E_{dc}.

bounce frequency,[25] through Eqs. (1) and (2). Thus, we can infer the bounce frequency from either the upper or lower sideband frequencies and wave numbers, as

$$\omega_B^{sb} = |\omega_T + \delta\omega_u - v_T k_u| \approx |\omega_T - \delta\omega_l - v_T k_l|, \tag{25}$$

where we use the measured values of the sideband wave numbers.

In Fig. 10 we compare this inferred bounce frequency with the bounce frequency ω_B^{dc} predicted for the measured trapping field strength, using Eq. (17). Experimentally we find in a best fit

$$\omega_B^{sb} \approx 0.7\omega_B^{dc}. \tag{26}$$

That is, the bounce frequency inferred from the sideband frequency separations is about 0.7 times the bounce frequency calculated from the dc field and trapping wave amplitude. This is probably caused by the finite extent of the trapped electron distribution in phase space, as seen in Fig. 4. Since the trapping potential is harmonic only near the bottom of the well, the average bounce frequency is reduced.

B. Properties of the sideband normal mode

The measured (and simulated) properties of the observed sideband normal modes (growth rates k^i, wave number shifts δk^r, modulational phase Θ, and amplitude ratio α) agree qualitatively (but not quantitatively) with the predictions of the MPM. The diamonds in Fig. 11 show the experimental measurements for different sideband frequencies, the crosses show the results from computer simulation, and the curves represent the MPM model. For the experiments and simulations, the growth rate and wave number shifts of the sideband normal modes are obtained by fitting straight lines to the measurements of the logarithms of the sideband amplitudes and to the measured phase shifts downstream where the sideband normal mode has become dominant.

For the model, the wave numbers k from the sideband dispersion relation of Eq. (18) are found numerically for given frequency ω. Typically we find two spatially growing solutions; however, one of them has a considerably smaller

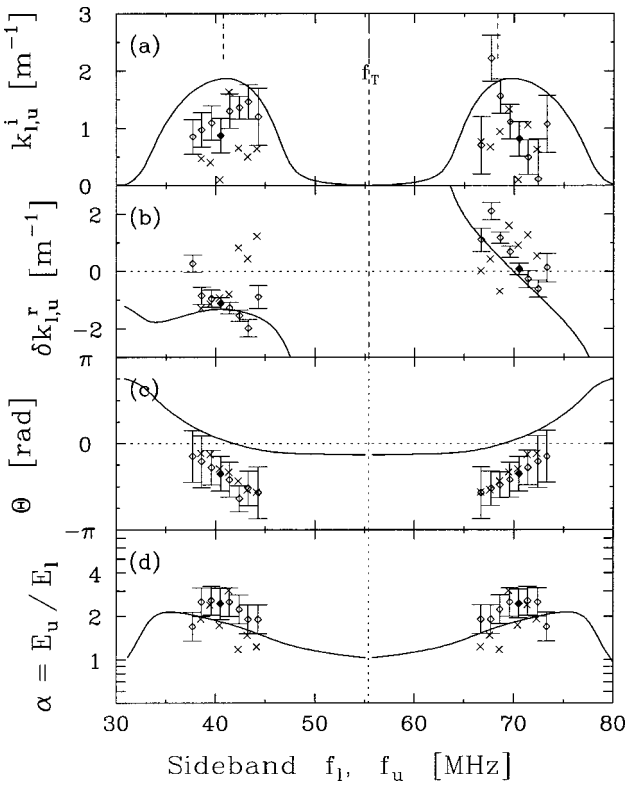

FIG. 11. Properties of the growing sidebands: growth rates k^i, wave number shifts δk^r, modulational phase Θ, and amplitude ratio α. Experiment ($\times$), computer simulation ($\diamond$), KDS dispersion relation (solid lines). The dashed vertical lines mark the sideband resonance frequencies.

growth rate k^i than the other, so we plot only the solution that has the largest growth rates. In the dispersion relation, we use the inferred ω_B^{sb}, and we use the measured wave numbers and damping rates of the beamless helix near the end of the interaction region. The trapped particle fraction is calculated from the measured velocity distribution function, according to Eq. (24). The velocity of the trapped macroparticle, i.e., the trapping wave phase velocity, is calculated from the measured wave number shift, δk_T^∞.

C. Dependence on helix dispersion relation

Sideband normal modes are only observed if the dispersion of the helix in the range of the trapping wave frequency is small. Sideband normal modes of the MPM have the property that since $\omega_u + \omega_l = 2\omega_T$, it follows that

$$k_u^r + k_l^r = 2k_T^\infty. \tag{27}$$

Since the helix dispersion does not satisfy Eq. (27), wave number changes $\delta k_{l,u}$ of both sidebands are necessary for a sideband normal mode to be observed. We characterize this total sideband shift by $\Delta k^{tot}/k_T^{0r} \equiv (2k_T^\infty - k_u^{0r} - k_l^{0r})/k_T^{0r}$.

Experimentally we only observe sideband normal modes if $\Delta k^{tot}/k_T^{0r} < 0.03$. This is illustrated in Fig. 12. For different frequencies of the trapping wave and of the upper sideband, the shading and the contour lines indicate the necessary wave number change, $\Delta k^{tot}/k_T^{0r}$, for a sideband normal mode to be observed. Obviously, this change depends on the wave number k_T^r of the trapping wave; the cases with different trapping

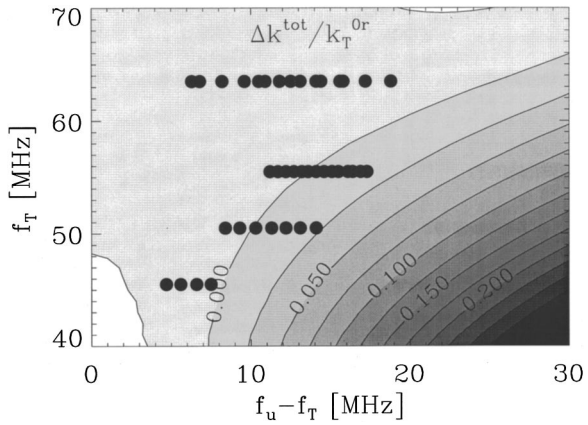

FIG. 12. Contour plot of the total sideband wave number shift $\Delta k^{\mathrm{tot}}/k_T^r$ required for a sideband normal mode. The wave number shift of the trapping wave is $\delta k_T^{\infty}=0.9\,\mathrm{m}^{-1}$. The dots are experimental conditions for which growing sidebands with constant modulational phase are observed.

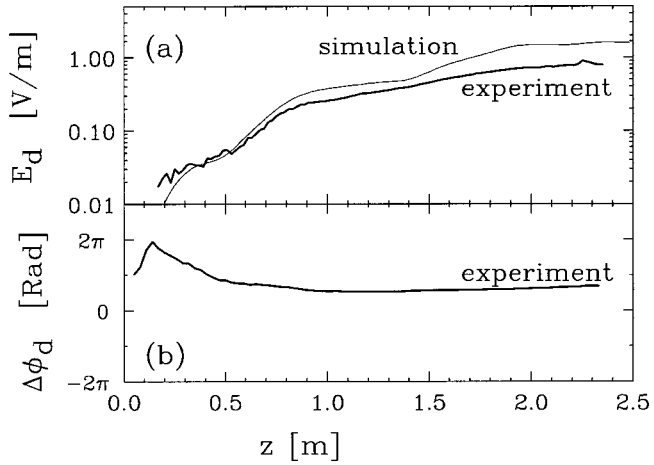

FIG. 13. Evolution of the amplitude E_d and nonlinear phase $\Delta\phi_d$ of the difference wave at $f=14.1$ MHz. The trapped particle state is that of Fig. 7.

wave frequencies were chosen to have the same wave number shift of the trapping wave, $\delta k_T=0.9\,\mathrm{m}^{-1}$, in order to enable plotting all cases on one graph. The dots show those cases for which we observe sideband normal modes. They all lie within the shaded region where $\Delta k^{\mathrm{tot}}/k_T^{0r}\lesssim 0.03$. Particularly at the lowest trapping wave frequency, we observe sideband normal modes only for small sideband frequency separations, where the necessary wave number changes of the sidebands are small.

Apparently the weak coupling between the sidebands (as already indicated by the small growth rates) is not able to manifest itself in an emerging sideband normal mode if the helix dispersion relation would require large wave number shifts.

D. Difference wave

Near the end of the interaction region, we observe not only the three launched waves but also some small nonlinear product waves. The strongest of these product waves is a ''difference'' wave with frequency $f_d=\delta f_{\mathrm{sb}}$. It is not phase related to the other waves, and its measured wave number cannot be explained within the framework of the MPM.

The spatial evolution of this difference wave is shown in Fig. 13, for a sideband evolution similar to that of Fig. 7. Close to the transmitter, the difference wave growth is rapid; but the growth diminishes with distance. The dashed line in Fig. 13 shows the result of a computer simulation where the difference wave was launched with an initial amplitude 40 dB below the initial amplitude of the sidebands. The agreement between the computer simulations and the experiment is good.

An obvious extension of the MPM theory is to include the difference wave in the linear system of equations that describe the coupling between the different frequencies of the electric field. This leads to a 3×3 rather than a 2×2 matrix. Setting the determinant to zero yields a new dispersion relation for the sidebands and the difference wave. For the sidebands, the growing solution is almost identical to the growing solution of the original dispersion relation. For the difference wave on the other hand, this dispersion relation predicts a growth rate that equals the growth rate of the sidebands, that is, $k_d^i=k_l^i=k_u^i$, and predicts a wave number given by $k_d=k_T^{\infty}-k_l^r$.

From Fig. 13 we can deduce the growth rate and the wave number shift of the difference wave. We find that the growth rate between $z=1.5\,\mathrm{m}$ and $z=2.3\,\mathrm{m}$ is $k_d^i\approx 0.3\,\mathrm{m}^{-1}$; this is comparable to the growth rate of the lower sideband, $k_l^i\approx 0.2\,\mathrm{m}^{-1}$. The observed wave number shift, however, is $\delta k_d^r\approx=0.5\,\mathrm{m}^{-1}$; this is not in agreement with the prediction of the expanded MPM model of $\delta k_d^r=k_T^{\infty}-k_l^r-k_d^{0r}\approx 16.8\,\mathrm{m}^{-1}$. In addition, the evolution is independent of the phases of either the upper or the lower sideband. Thus, the growth of this difference wave is probably caused by the untrapped (fast) electrons and not by some parametric coupling process that involves the trapped electrons.

VI. SUMMARY

We have characterized the asymptotic trapped-particle states on a traveling wave tube and compared the measurements to a simple macroparticle model and to computer simulations. In the experiments, the monoenergetic electron beam is trapped by a launched large amplitude wave, and a dc electric field maintains the state against damping. By suitably choosing the launch level of the trapping wave, we obtain states with constant wave amplitude over the length of the experiment.

The measured fraction of trapped electrons agrees with the prediction of the macroparticle model, whereas the measured wave number shift is smaller than predicted. When small amplitude sideband waves are launched, they grow for frequencies that approximately fulfill the sideband resonance condition. The bounce frequency of the trapped macroparticle inferred from the frequency of the fastest growing sidebands is only about 70% of the bounce frequency calculated from the wave trapping amplitude.

The upper and lower growing sidebands are strongly coupled if the dispersion relation allows wave number matching of the sidebands with the trapping wave. This coupling manifested itself in the formation of a sideband normal

mode. The measured growth rates, wave number shifts, amplitude ratio, and phase relationship of the sidebands agree only qualitatively with the sideband normal mode predictions of the MPM. Better quantitative agreement is found between the experiment and computer simulations that follow the orbits of a distribution of beam electrons. Therefore we conclude that the quantitative discrepancies between the measured properties of the sideband normal modes and the predictions of the MPM arise from the approximation of trapped electrons as a single macroparticle; for quantitative predictions, the field phase-space dynamics must be kept.

ACKNOWLEDGMENT

This work was supported by National Science Foundation Grant No. PHY-9876999.

[1]C. B. Wharton, J. H. Malmberg, and T. M. O'Neil, Phys. Fluids **11**, 1761 (1968).
[2]R. N. Franklin, S. M. Hamberger, H. Ikezi, G. Lampis, and G. J. Smith, Phys. Rev. Lett. **28**, 114 (1972).
[3]P. DeNeef, Phys. Rev. Lett. **31**, 446 (1973).
[4]G. Jahns and G. Van Hoven, Phys. Rev. Lett. **31**, 436 (1973).
[5]G. Van Hoven and G. Jahns, Phys. Fluids **18**, 80 (1975).
[6]P. DeNeef, Phys. Fluids **18**, 1209 (1975).
[7]R. N. Franklin and R. R. MacKinlay, Phys. Fluids, **19**, 173 (1976).
[8]R. N. Franklin, R. R. MacKinlay, P. D. Edgley, and D. N. Wall, Proc. R. Soc. London, Ser. A **360**, 229 (1978).
[9]M. Bitter and P. J. Paris, J. Plasma Phys. **14**, 389 (1975).
[10]W. Carr, D. Boyd, H. Liu, G. Schmidt, and M. Seidl, Phys. Rev. Lett. **28**, 662 (1972).
[11]K. Mizuno and S. Tanaka, Phys. Rev. Lett. **29**, 45 (1972).
[12]K. Jungwirth, V. Piffl, and J. Ullschmied, Plasma Phys. **16**, 283 (1974).
[13]P. DeNeef, J. H. Malmberg, and T. M. O'Neil, Phys. Rev. Lett. **30**, 1032 (1973).
[14]G. Dimonte and J. H. Malmberg, Phys. Fluids **21**, 1188 (1978).
[15]Y. Sakawa and C. Joshi, Phys. Plasmas **7**, 1774 (2000).
[16]R. W. Warren, B. E. Newnam, and J. C. Goldstein, IEEE J. Quantum Electron. **QE-21**, 882 (1985).
[17]R. Brian and R. Davidson, Phys. Fluids B **2**, 2456 (1990).
[18]S. Riyopoulos, Phys. Fluids B **3**, 2684 (1991).
[19]D. Shiffler, J. D. Ivers, G. S. Kerslick, J. A. Nation, and L. Schachter, Appl. Phys. Lett. **58**, 899 (1991).
[20]W. L. Kruer and J. M. Dawson, Phys. Fluids **13**, 2747 (1970).
[21]J. Denavit and W. L. Kruer, Phys. Fluids **14**, 1782 (1971).
[22]Y. Matsuda and F. W. Crawford, Phys. Fluids **18**, 1346 (1975).
[23]M. M. Shoucri, Phys. Fluids **21**, 1359 (1978).
[24]B. P. Koch and R. W. Leven, Phys. Scr. **27**, 220 (1982).
[25]S. I. Tsunoda and J. H. Malmberg, Phys. Fluids B **1**, 1958 (1989).
[26]W. L. Kruer, J. M. Dawson, and R. N. Sudan, Phys. Rev. Lett. **23**, 838 (1969).
[27]G. J. Morales, Phys. Fluids **23**, 2472 (1980).
[28]V. L. Krasovsky, Phys. Scr. **49**, 489 (1994).
[29]K. Mima and K. Nishikawa, Phys. Soc. Jpn. **33**, 1669 (1972).
[30]J. R. Pierce, *Traveling-Wave Tubes* (Van Nostrand, New York, 1950).
[31]S. I. Tsunoda and J. H. Malmberg, Phys. Fluids **27**, 2557 (1984).
[32]D. A. Hartmann, Ph.D. thesis, University of California, San Diego, 1994.
[33]D. A. Hartmann, C. F. Driscoll, T. M. O'Neil, and V. D. Shapiro, Phys. Plasmas **2**, 654 (1995).